Soils and Rocks
An International Journal of Geotechnical and Geoenvironmental Engineering
www.soilsandrocks.com
ISSN 1980-9743
ISSN-e 2675-5475

Pseudo-static analysis of tunnel face stability using the Mohr-Coulomb strength criterion

Zied Saada[1#], Denis Garnier[2], Samir Maghous[3]

Article

Keywords
Tunnel face stability
Mohr-Coulomb criterion
Limit analysis
Seismic loading

Abstract

The paper addresses the stability analysis of a circular tunnel face driven by a pressurized shield by means of the limit analysis kinematic approach implemented in the context of the Mohr-Coulomb strength condition. Emphasis is given to the assessment of the effects of seismic loading on the value of face support pressure that is required to prevent failure. The approach relies upon the pseudo-static method to model the destabilizing effects induced by the inertial forces associated with the passage of seismic waves in the ground. Rigorous limit analysis solutions for the limit face supporting pressure are derived from the analytical implementation of 3D and 2D failure mechanisms specifically devised for dealing with such a stability analysis problem. Indeed, original analytical expressions are provided and allow the evaluation of the pressure stabilizing the tunnel face. The accuracy of the approach predictions is assessed by comparison with available experimental and analytical results as well as with 2D finite element solutions. The influence of some relevant problem parameters in the context of tunnel face stability analysis is finally investigated, thus providing some preliminary guidelines for practical use in tunnel engineering.

1. Introduction

The stability of the tunnel face is a major issue in tunnel excavation. Both experimental and theoretical analysis were performed in order to assess this problem, since the early paper by Broms & Bennermark (1967) that was based on laboratory tests and field observations.

Some authors performed excavations of microtunnels (Pellet et al.,1993; Lee et al., 2003) and Lee & Shubert (2008)). Such experiments can only give qualitative results because of the scale effect. Other authors introduced microtunnels in centrifuges in order to increase the dimensions of the prototypes by the levels of accelerations used (Chambon & Corté, 1990, 1994; Kamata & Mashimo, 2003; Hisatake et al., 2009; Juneja et al., 2010 among others).

Large scale experiments were carried out by Shin et al. (2008) and Askoy & Onargan (2010). It was proved that the umbrella arch and face bolt applications have significantly reduced the ground settlements.

On the other hand, several research papers were devoted to the theoretical study of tunnel face stability. Some authors considered a 2D geometry and the problem was investigated under plane strain conditions (Funatsu et al., 2008; Tschuchnigg et al., 2015; Xu et al., 2015; Yang et al., 2016; Huang et al., 2018; Zhang et al., 2018, 2019a; Man et al. (2022), among others). While for other researchers, a 3D geometry was considered (De Buhan et al., 1999; Leca & Dormieux, 1990; Cuvillier, 2001; Mollon et al., 2010, 2013; Zhang et al., 2015, 2017; Saada et al., 2013, to cite a few). It should be noted that the study of tunnel face stability as a two-dimensional problem could be useful as a first approach. This study is relatively simple and allows the understanding of the studied subject. Then, it is necessary to investigate the three-dimensional problem which can provide more realistic results.

Moreover, as regards the effect of seepage forces on tunnel face stability, this topic was investigated by several authors (Xu et al., 2015; Yang et al., 2016; De Buhan et al., 1999; Cuvillier, 2001; Chen et al., 2022; Zhang et al., 2019b, among others). They proved that water seepage forces could considerably reduce the stability of the tunnel. The amount of reduction depends on: the soil permeability, the velocity of the tunnel face, the level of water table, etc.

In addition, the behavior of tunnel face reinforced by longitudinal pipes, bolts or nails, or umbrella arch was also investigated (Kamata & Mashimo, 2003; Juneja et al., 2010; Shin et al., 2008; Askoy & Onargan, 2010; Funatsu et al., 2008; Zhang et al., 2018; Cuvillier, 2001 and Paternesi et al., 2017, to cite a few). It was proved that such a reinforcement could increase the tunnel face stability.

Moreover, several theoretical methods were used in order to investigate the stability of the tunnel face (finite element,

[#]Corresponding author. E-mail address: zied.saada@enit.utm.tn
[1]Université de Tunis El Manar, Ecole Nationale d'Ingénieurs de Tunis, Laboratoire de Génie Civil, Tunis, Tunisia.
[2]Université Gustave Eiffel, Ecole des Ponts ParisTech, Laboratoire Navier CNRS UMR, Marne-la-Vallée, France.
[3]Universidade Federal do Rio Grande do Sul, Departamento de Engenharia Civil, Porto Alegre, RS, Brasil.

Submitted on December 12, 2023; Final Acceptance on September 13, 2024; Discussion open until May 31, 2025.
Editor: Renato P. Cunha
https://doi.org/10.28927/SR.2025.011423

finite difference, limit analysis). Among these methods, limit analysis theory was considered in some research papers.

In the sequel, some contributions based on limit analysis theory will be described. Davis et al. (1980) presented a stability criterion for cohesive soils, that accounts for the effects of tunnel depth. The derived criterion was supported by centrifuge experiments (Schofield, 1980). The same problem was investigated by Dormieux & Leca (1993) and Leca & Dormieux (1992). In some situations of profound tunnels, they found better lower bound estimates, of the pressure applied to the tunnel face, than Davis et al. (1980).

More recently, Mollon et al. (2013) proposed two new continuous velocity fields for both collapse and blowout of a tunnel face. The obtained numerical results improved the best existing bounds for collapse pressures.

As far as frictional materials are concerned, face stability of tunnels driven in such dry or saturated materials was also investigated (Pan & Dias, 2018; Zhao et al., 2017; Cheng et al., 2019; Zou et al., 2019; Li & Yang, 2019, among others).

Recently, several researchers have studied the face stability of tunnel excavated in a Mohr-Coulomb soil, taking into account the seismic acceleration (Zhang et al., 2017, 2020, 2021; Zhong & Yang, 2020; Hou & Yang, 2020; Chen et al., 2023).

Zhang et al. (2017) constructed a three-dimensional failure mechanism and took into consideration the seismic acceleration by the quasi-static method. The nonlinear Mohr-Coulomb criterion was introduced into the limit analysis using the tangent technique. Their results showed that the nonlinear coefficient and the initial cohesion have a significant effect on the collapse pressure and the failure zone.

Moreover, Zhang et al. (2020) combined the response surface method and the limit analysis to study the reliability of tunnel face subjected to seismic acceleration. The applied pressure to the tunnel face was evaluated using the kinematic approach of limit analysis. In addition, the influence of several parameters on the obtained results was investigated.

On the other hand, Zhong & Yang (2020) used the kinematic approach of limit analysis to study the seismic stability of tunnel face. The pseudodynamic method was considered in order to model the seismic acceleration and a three-dimensional failure mechanism was taken into consideration. Finally, a parametric study was carried out to investigate the effects of various parameters on the retaining force.

Furthermore, Zhang et al. (2021) studied the effects of seismic accelerations on the active and passive failures of tunnel face. The kinematic approach of limit analysis was considered and the seismic acceleration was taken into account using the pseudo static method. This study provided more reasonable and effective values for the supporting pressure of tunnel face.

In addition, Hou & Yang (2020) used a tension cut-off in the Mohr-Coulomb failure criterion in order to study the seismic stability of tunnel face. A parametric study and stability charts were presented in the paper.

On the other hand, Chen et al. (2023) studied the seismic stability of the tunnel face in heterogeneous and anisotropic soil. They used the pseudodynamic method to take into account seismic acceleration.

Finally, it should be noted that in all these research papers mentioned above of seismic stability of tunnel face, the pressure applied to the tunnel face was numerically evaluated. Indeed, the work rates of external forces and the work rates of energy dissipation were given as integrals. Furthermore, these integrals were numerically evaluated.

In this context, this paper studies the face stability of a tunnel excavated in a Mohr-Coulomb soil in the presence of seismic acceleration. The kinematic approach of limit analysis is considered for solving the problem. A semi-analytical calculation is carried out in order to evaluate a lower bound of the pressure applied to the tunnel face. 3 failure mechanisms are used: 2 three-dimensional mechanisms (cone mechanism and horn mechanism) as well as a two-dimensional failure mechanism. Moreover, most of expressions of the work rates of external forces and the maximum resisting work rates, related to failure mechanisms presented in this paper, are analytically evaluated. Finally, comparisons are made with numerical solutions obtained using the OptumG2 software as well as with results from the literature.

2. Statement of the problem

The objective of this paper is to calculate a lower bound estimate of the tunnel face collapse pressure σ_T. Figure 1 presents the geometry of the 3D analyzed problem.

The soil is subjected to gravity acceleration γ and seismic acceleration $k_h\gamma$. A uniform pressure σ_T is applied to the front of the tunnel. It is assumed that the tunnel is shield driven. The circular rigid impervious tunnel of diameter D is driven under a depth of cover H. Besides, the tunnel lining is assumed to be stable. In addition, the soil is assumed to be homogeneous and isotropic.

Furthermore, the tunnel is assumed deep enough to suppose that collapse of the tunnel face is associated to local failure mechanisms that are not reaching the upper ground surface.

The applied face pressure σ_T is assumed to be uniformly distributed along the tunnel face. This constant pressure can be applied by shield tunnelling under compressed air. However, the assumption of constant pressure σ_T allows also for approximate results for the stability problem of the tunnel driven by using techniques such as slurry or earth balance shields, both in terms of failure mechanisms and limit pressure.

In the present investigation, the acceleration within the soil mass is accounted for through the concept of average seismic coefficient (Seed, 1979). Only the horizontal component of seismic acceleration is considered in the present analysis.

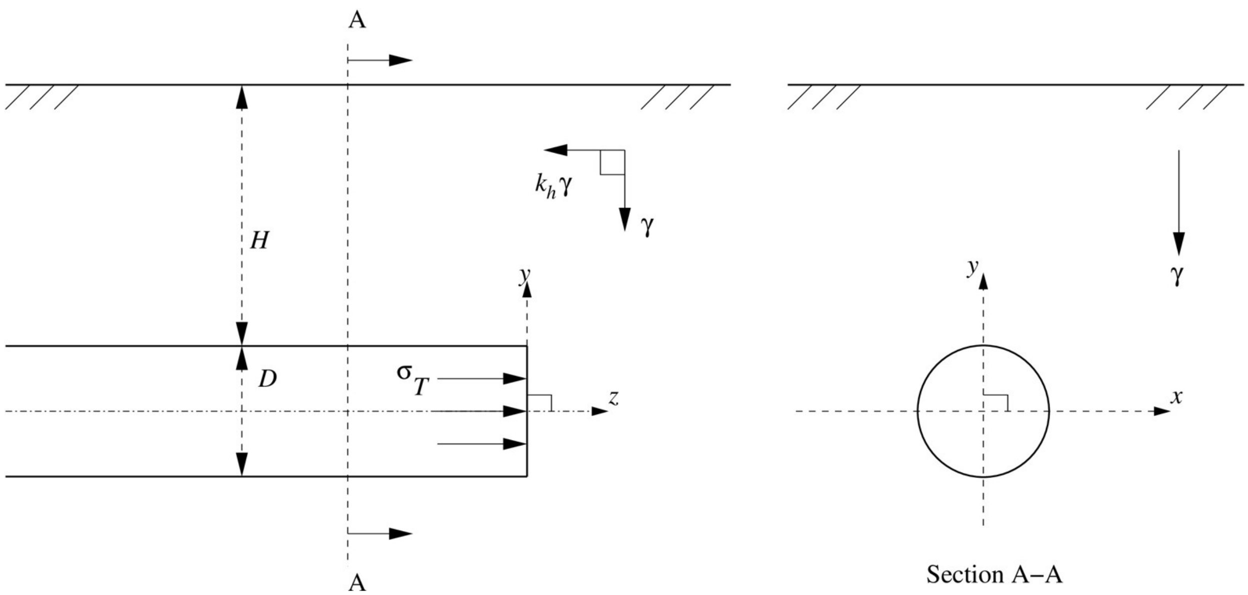

Figure 1. Problem geometry and loading mode.

Furthermore, it is assumed that the horizontal distribution of acceleration is uniform within the soil mass.

On the other hand, the effects of pore water pressure are not considered in the present contribution.

In this paper, the strength capacity of the soil is assumed to be described by the Mohr-Coulomb failure criterion.

$$F\left(\underline{\underline{\sigma}}\right) = \underbrace{\max}_{i,j\in\{1,2,3\}}\begin{bmatrix}\sigma_i\left(1+\sin\left(\varphi\right)\right)- \\ \sigma_j\left(1-\sin\left(\varphi\right)\right)-2c\cos\left(\varphi\right)\end{bmatrix}\leq 0 \quad (1)$$

Where c and φ are the Mohr-Coulomb strength parameters, and σ_1, σ_2 and σ_3 are the principal stresses (stresses are counted positive in tensile).

3. Limit analysis kinematic approach and support functions of The Mohr-Coulomb criterion

Kinematic approach of limit analysis can be used in order to obtain upper bound estimates of the extreme loads acting on a given structure (Salençon, 1983, 1990).

This approach indicates that for any virtual kinematically admissible velocity field $\underline{U}$, a necessary condition for the structure to remain safe, is that the work rate of external loads does not exceed the rate of maximum resisting work. This condition can be written as follows:

$$P_{ext}\left(\gamma, k_h\gamma, \sigma_T, \underline{U}\right)\leq P_{mr}\left(\underline{U}\right) \quad \forall\, \underline{U} \text{ kinematically admissible} \quad (2)$$

In the above inequality, $\underline{U}$ is a kinematically admissible velocity field which is in accordance with the boundary conditions. In addition, $P_{ext}\left(\gamma, k_h\gamma, \sigma_T, \underline{U}\right)$ is the work rate of external loads, and $P_{mr}\left(\underline{U}\right)$ is a positive quantity called the rate of maximum resisting work. It can be written as:

$$P_{mr}\left(\underline{U}\right)=\int_{\Omega}\Pi\left[\underline{\underline{d}}\left(\underline{x}\right)\right]d\Omega+\int_{\Sigma}\Pi\left[\underline{\upsilon}\left(\underline{x}\right),\left[\underline{U}\left(\underline{x}\right)\right]\right]d\Sigma \quad (3)$$

In the above expression, $\underline{\underline{d}}$ is the strain rate field associated with $\underline{U}$, and $\left[\underline{U}\right]$ is the jump when crossing a velocity discontinuity surface Σ having a normal unit vector $\underline{\upsilon}$. Ω is the soil volume.

The Π-functions, also called support functions, are defined by the following equations:

$$\Pi\left[\underline{\underline{d}}\right]=\underbrace{\text{Sup}}_{\underline{\underline{\sigma}}}\left\{\underline{\underline{\sigma}}:\underline{\underline{d}}\,\middle|\,F\left(\underline{\underline{\sigma}}\right)\leq 0\right\} \quad (4)$$

$$\Pi\left[\underline{\upsilon},\left[\underline{U}\right]\right]=\underbrace{\text{Sup}}_{\underline{\underline{\sigma}}}\left\{\left[\underline{U}\right].\underline{\underline{\sigma}}.\underline{\upsilon}\,\middle|\,F\left(\underline{\underline{\sigma}}\right)\leq 0\right\} \quad (5)$$

The Π-functions of the Mohr-Coulomb criterion are given by Salençon (1983).

A velocity field is relevant (i.e. $\Pi\left[\underline{\underline{d}}\right]<+\infty$) if the associated strain rate $\underline{\underline{d}}$ satisfies the following condition

$$tr\left(\underline{\underline{d}}\right)\geq\left(\left|d_1\right|+\left|d_2\right|+\left|d_3\right|\right)\sin\left(\varphi\right) \quad (6)$$

In which d_1, d_2 and d_3 represent the eigenvalues of $\underline{\underline{d}}$.

If the previous condition is satisfied, $\Pi\left[\underline{\underline{d}}\right]$ is expressed as:

$$\Pi\left[\underline{\underline{d}}\right]=\frac{c}{\tan(\varphi)}tr\left(\underline{\underline{d}}\right) \tag{7}$$

Besides, the relevancy condition in terms of velocity jump reads:

$$\left[\underline{U}\right].\underline{\upsilon}\geq\left\|\left[\underline{U}\right]\right\|\sin(\varphi) \tag{8}$$

If the velocity field $\underline{U}$ satisfies the relevancy condition expressed above, function $\Pi\left[\underline{\upsilon},\left[\underline{U}\right]\right]$ equals

$$\Pi\left[\underline{\upsilon},\left[\underline{U}\right]\right]=\frac{c}{\tan(\varphi)}\left[\underline{U}\right].\underline{\upsilon} \tag{9}$$

In the following section, the work rate of external loads and the rate of maximum resisting work are calculated for the considered failure mechanisms. This approach enables the calculation of a lower bound of the limit supporting pressure σ_T applied to the tunnel face which is necessary to prevent its failure.

4. Failure mechanisms

The aim of this paper is to compute a lower bound of the pressure σ_T applied to the tunnel face in order to stabilize it. In order to achieve this objective, the study is carried out using the kinematic approach of limit analysis.

Chambon & Corté (1994) introduced in centrifuge microtunnels driven in sands, and obtained failure envelope bulb-shaped in all cases of shallow and deep tunnels. They observed that in cases of deep tunnel, the bulb closes and the stability of the soil is ensured by arching and load transfer to the crown of the tunnel.

The research investigation presented in this paper takes into account the experimental results obtained by Chambon & Corté (1994). Three local failure mechanisms are considered in this paper: cone mechanism introduced by Leca & Dormieux (1990), horn mechanism introduced by Cuvillier (2001) and 2D mechanism introduced by Chambon & Corté (1990).

Furthermore, it is interesting to notice that Leca & Dormieux (1990) obtained a good agreement between the theoretical estimate derived from kinematic approach of limit analysis and measured face pressure from centrifuge experiments performed by Chambon & Corté (1989).

Within this context, the kinematic approach developed in the subsequent analysis shall provide rigorous lower bound estimates for the pressure σ_T applied to the tunnel face that would be necessary for preventing its failure.

4.1 Cone translational failure mechanism

The failure mechanism used in this section was originally introduced by Leca & Dormieux (1990). It should be noted that Leca & Dormieux (1990) did not consider seismic acceleration in the ground. Furthermore, the geometry of cone mechanism is presented in Figure 2. For the considered mechanism, the zone in motion is a cone with circular cross-section and an opening angle equal to 2φ. The angle between the cone axis (ΩZ) and the tunnel axis (Oz) is α.

The cone in motion translates as a rigid body with a uniform velocity $\underline{v}$ which is parallel to its axis. The considered cone mechanism depends only on one parameter which is α. Furthermore, it should be noticed that the intersection of the tunnel with the cone is an ellipse Σ the major axis of which is equal to $D/2$ (Figure 2). Finally, it should be noted that the geometric quantities related to cone mechanism are presented in Appendix A.

The rate of external loads work is the sum of three contributions (tunnel face pressure σ_T, unit weight γ and seismic acceleration $-k_h\gamma\underline{e}_z$):

$$P_{ext}=P_{\gamma}+P_{k_h\gamma}+P_{\sigma_T} \tag{10}$$

In the above equation, P_{σ_T} is the work rate of face pressure σ_T, P_{γ} is the work rate of the soil unit weight γ and $P_{k_h\gamma}$ is the work rate of the seismic acceleration $-k_h\gamma\underline{e}_z$.

The three work rates involved in Equation 10 are given by:

$$P_{\gamma}=\iiint_{V-cone}\left(-\gamma\underline{e}_y\right).\left(v\underline{e}_Z\right)dV=D^3\gamma v f_1 \tag{11}$$

$$P_{k_h\gamma}=\iiint_{V-cone}\left(-k_h\gamma\underline{e}_z\right).\left(v\underline{e}_Z\right)dV=k_hD^3\gamma v f_1' \tag{12}$$

$$P_{\sigma_T}=\iint_{\Sigma}\left(\sigma_T\underline{e}_z\right).\left(v\underline{e}_Z\right)d\Sigma=-D^2\sigma_T v f_2 \tag{13}$$

In which Σ is the area of intersection between the cone and the tunnel face, and *V-cone* refers to the volume of the translational conical block. The dimensionless functions f_1, f_1' and f_2 are given in Appendix A.

Taking into account Equations 11-13, we can calculate the following expression of P_{ext}:

$$P_{ext}=D^3\gamma v\left(f_1+k_hf_1'\right)-D^2\sigma_T v f_2 \tag{14}$$

Observing that the cone moves like a rigid body, the expression of the rate of maximum resisting work results therefore only from the contribution related to the velocity jump along the lateral surface *A-lateral* of the cone.

$$P_{mr}=\iint_{A-lateral}\Pi\left[\underline{\upsilon}(\underline{x}),\left[\underline{U}(\underline{x})\right]\right]d\Sigma=cvD^2f_3 \tag{15}$$

Where f_3 is a dimensionless function given in Appendix A.

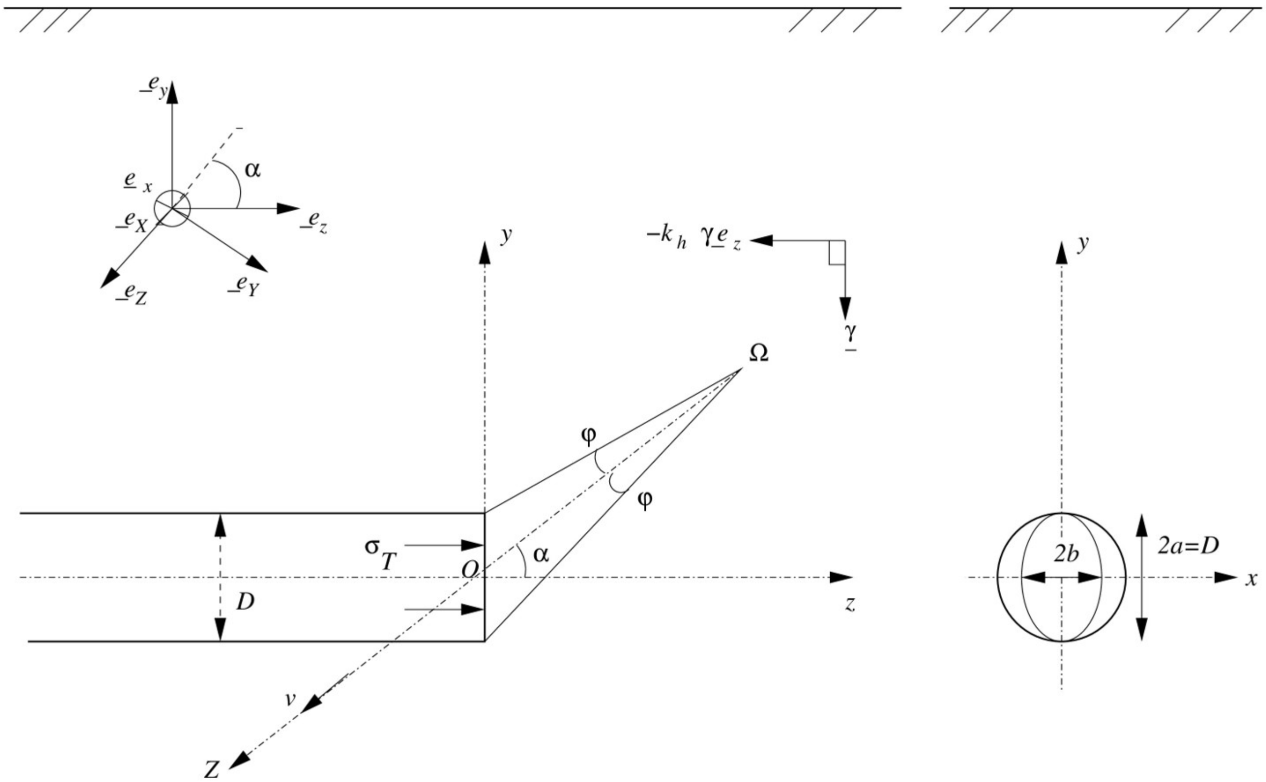

Figure 2. Cone failure mechanism.

Using the upper bound theorem of limit analysis which states that $P_{ext} \leq P_{mr}$, one obtains a lower bound estimate of the applied pressure:

$$\frac{\sigma_{T1}}{\gamma D} = \underbrace{\text{Max}}_{\alpha}\left[\left(\frac{f_1 + k_h f_1'}{f_2}\right) - \frac{c}{\gamma D}\frac{f_3}{f_2}\right] \leq \frac{\sigma_T}{\gamma D} \qquad (16)$$

The value of the tunnel face pressure σ_{T1} represents the best lower bound estimate of σ_T that can be obtained from exploring the above class of cone mechanism through a maximization procedure with respect to the angular parameter α. The latter maximization procedure is carried out numerically.

Finally, it should be noted that angular parameter α is subjected to the following constraint

$$0 \leq \alpha < \frac{\pi}{2} - \varphi \qquad (17)$$

4.2 Three-dimensional Horn-shaped rotational failure mechanism

The second failure mechanism considered in this paper is the horn-like rotational failure mechanism depicted in Figure 3, which was originally developed by Cuvillier (2001). It should be noted that Cuvillier (2001) did not consider seismic acceleration in the ground. It should be underlined that this 3D failure mechanism has been developed based on the 2D failure mechanism presented by Chambon & Corté (1990) and described in the next section.

Before further developments regarding the implementation of kinematic approach, it may be convenient to first define the geometry of this failure mechanism in the vertical plane *(Oyz)*, which represents a plane of symmetry for the tunnel passing through the tunnel axis. In the plane *(Oyz)*, points A and C are respectively located at the crown and the invert of the tunnel face. The cross-section of the rotational horn block in the considered plane is delimited by two log-spiral curves *AB* and *CB* defined with respect to the same focus Ω and opposite angles + and $-\varphi$. Located in the tunnel plane of symmetry, the cartesian coordinates of focus Ω are:

$$x_\Omega = 0 \quad , \quad y_\Omega = (\beta + 1/2)\,D \quad , \quad z_\Omega = -\alpha\, D \qquad (18)$$

Parameters α and β are positive scalars.

The log-spiral curves *AB* and *CB* are respectively defined in the cylindrical coordinate system $(\Omega, \underline{e}_r, \underline{e}_\theta, \underline{e}_Z)$ with $\underline{e}_Z = -\underline{e}_x$ by:

$$r_A(\theta) = D\sqrt{\alpha^2 + \beta^2}\, e^{\tan(\varphi)(\theta - \theta_A)} \qquad (19)$$

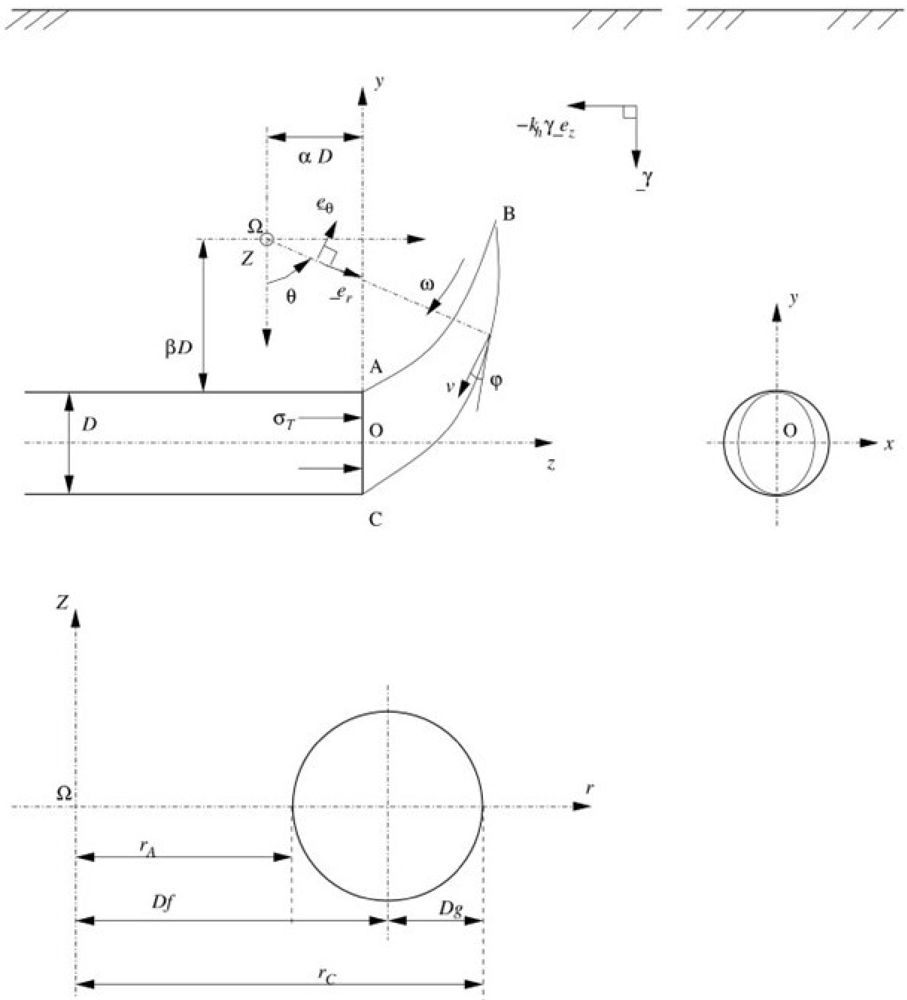

Figure 3. three-dimensional horn-shaped rotational failure mechanism.

$$r_C\left(\theta\right)=D\sqrt{\alpha^2+\left(1+\beta\right)^2}\,e^{\tan\left(\varphi\right)\left(\theta_C-\theta\right)} \tag{20}$$

In the above equations, θ_A and θ_C are respectively the polar orientation of points A and C. The polar orientation θ_B of point B is deduced from equality $r_A\left(\theta=\theta_B\right)=r_C\left(\theta=\theta_B\right)$. One can deduce the following expression of θ_B:

$$\theta_B=\frac{\theta_A+\theta_C}{2}+\frac{1}{2\tan\left(\varphi\right)}Ln\left(\frac{\sin\left(\theta_A\right)}{\sin\left(\theta_C\right)}\right) \tag{21}$$

From a three-dimensional viewpoint, the horn-shaped volume is bounded by the tunnel face and a parametric surface *J*. The latter is defined as the envelope of the circles located in the plane $\left(\Omega,\underline{e}_r,\underline{e}_Z\right)$, delimited by the logarithmic spiral curves *AB* and *CB*, and rotating around axis $\left(\Omega,\underline{e}_Z\right)$. The parametric surface *J* is defined in the cylindrical coordinates by the following equation:

$$\begin{gathered}M\in J\Leftrightarrow\exists\left(\theta,t\right)\in\left[0,2\pi\right]^2/\,\underline{\Omega M}=\\ D\left[f\left(\theta\right)+g\left(\theta\right)\cos\left(t\right)\right]\underline{e}_r+Dg\left(\theta\right)\sin\left(t\right)\underline{e}_Z\end{gathered} \tag{22}$$

The dimensionless functions *f* and *g* are given by

$$f\left(\theta\right)=\frac{r_C\left(\theta\right)+r_A\left(\theta\right)}{2D} \tag{23}$$

$$g\left(\theta\right)=\frac{r_C\left(\theta\right)-r_A\left(\theta\right)}{2D} \tag{24}$$

We move now to the description of velocity field associated with the horn-like failure mechanism. In this failure mechanism, the rigid horn-shaped block is given a rotational rigid body motion defined by angular velocity $-\omega\,\underline{e}_Z$. The axis of rotation of the horn block is $\left(\Omega Z\right)$. The remaining part of the soil is kept motionless. The velocity of any point M belonging to the horn block is therefore given in the cylindrical coordinate system $\left(\Omega, r, \theta, Z\right)$ by

$$\underline{v} = -\omega r \underline{e}_{\theta} \tag{25}$$

It is first observed that the above failure mechanism involves a velocity jump along surface J separating the moving block and the remaining motionless ground: $\left[\underline{U}\right] = \underline{v} = -\omega\, r\, \underline{e}_{\theta}$. The latter velocity jump is inclined for any value of θ at angle φ with respect to the discontinuity surface J, thus complying with the relevancy condition (8).

The application of the fundamental inequality (2) of limit analysis kinematic approach requires computing both the rate of maximum resisting work and the work rate of external loads developed in the considered failure mechanism. In that respect, it is noted that full details related to the derivation of P_{mr} and P_{ext} expressions are provided in Appendix B.

Keeping in mind that the horn block rotates as a rigid body, the rate of maximum resisting work reduces to the contribution of the velocity jump along surface J:

$$P_{mr} = \iint_J \Pi\left(\underline{\upsilon}, \left[\underline{U}\right]\right) d\Sigma = c\omega D^3 \left(g_1 + g_2\right) \tag{26}$$

in which g_1 and g_2 are dimensionless functions provided in the Appendix B.

The rate of external loads work comprises the contributions of face supporting pressure σ_T, unit weight γ and seismic acceleration $-k_h \gamma \underline{e}_z$:

$$P_{ext} = P_{\gamma} + P_{k_h\gamma} + P_{\sigma_T} \tag{27}$$

The work rates involved in the equation above are expressed as:

$$P_{\gamma} = \iiint_{V-horn} \left(-\gamma \underline{e}_y\right) . \left(-\omega r \underline{e}_{\theta}\right) dV = \gamma \omega D^4 \left(g_3 + g_4\right) \tag{28}$$

$$P_{k_h\gamma} = \iiint_{V-horn} \left(-k_h \gamma \underline{e}_z\right) . \left(-\omega r \underline{e}_{\theta}\right) dV = k_h \gamma \omega D^4 \left(g'_3 + g'_4\right) \tag{29}$$

$$P_{\sigma_T} = \iint_{\Sigma} \left(\sigma_T \underline{e}_z\right) . \left(-\omega r \underline{e}_{\theta}\right) d\Sigma = -\sigma_T \omega D^3 g_5 \tag{30}$$

where surface Σ is the intersection between the tunnel face and the horn volume, and *V-horn* refers to the volume of the horn-like in rotation. The dimensionless functions g_3, g_4, g'_3, g'_4 and g_5 are provided in the Appendix B.

It follows from applying inequality (2) of the limit analysis kinematic approach that:

$$\frac{\sigma_{T2}}{\gamma D} = \underset{(\theta_C, \theta_A)}{\mathrm{Max}} \left[\left(\frac{g_3 + g_4}{g_5} + k_h \frac{g'_3 + g'_4}{g_5} \right) - \frac{c}{\gamma D} \frac{g_1 + g_2}{g_5} \right] \leq \frac{\sigma_T}{\gamma D} \tag{31}$$

σ_{T2} represents the best lower bound estimate of σ_T which can be obtained from exploring the class of horn-shaped failure mechanisms through a maximization procedure with respect to the angular paramaters θ_C and θ . These angular variables have to comply with the following contraints:

$$0 < \theta_C < \theta_A \leq \frac{\pi}{2} \tag{32}$$

$$\theta_A < \theta_B = \frac{\theta_A + \theta_C}{2} + \frac{1}{2\tan\left(\varphi\right)} \mathrm{Ln}\left(\frac{\sin\left(\theta_A\right)}{\sin\left(\theta_C\right)} \right) < \frac{3\pi}{2} \tag{33}$$

4.3 Two-dimensional horn-like failure mechanism of Chambon & Corté (1990)

With the purpose to compare the results of kinematical approach with 2D finite element solutions, the stability analysis problem under plane strain conditions parallel to the vertical plane *(Oyz)* is addressed herein by means of the two-dimensional failure mechanism proposed by Chambon & Corté (1990). The latter is extended in the subsequent analysis to the situation of seismic acceleration in the ground. The geometry of studied stability problem is sketched in Figure 4.

Description of this 2D horn-like failure mechanism, which is depicted in Figure 5, is identical to that of the 3D counterpart failure mechanism in the vertical plane *(Oyz)*. The horn block *ABC* is endowed with a rotational motion $-\omega\, \underline{e}_Z$ about $\left(\Omega Z\right)$ axis, while the remaining part of the soil is kept motionless. Referring to the notation of figure 5, the equations of the log-spiral curves *AB* and *CB* of focus $\Omega\left(y_{\Omega} = \left(\beta + 1/2\right) D, z_{\Omega} = -\alpha\, D\right)$ and angles $\pm\varphi$ are still given respectively by Equations 19 and 20.

The rate of external loads work developed in the failure mechanism by the pressure (by transverse length) σ_T, gravity forces $-\gamma \underline{e}_y$ and seismic acceleration $-k_h \gamma \underline{e}_z$ reads

$$P_{ext} = P_{\gamma} + P_{k_h\gamma} + P_{\sigma_T} \tag{34}$$

Where

$$P_{\gamma} = \iint_S \left(-\gamma \underline{e}_y\right) . \left(-\omega r \underline{e}_{\theta}\right) dS = \gamma \omega D^3 \left(h_1 + h_2\right) \tag{35}$$

$$P_{k_h\gamma} = \iint_S \left(-k_h \gamma \underline{e}_z\right) . \left(-\omega r \underline{e}_{\theta}\right) dS = k_h \gamma \omega D^3 \left(h_3 + h_4\right) \tag{36}$$

$$P_{\sigma_T} = \int_{[CA]} \left(\sigma_T \underline{e}_z\right) . \left(-\omega r \underline{e}_{\theta}\right) dy = -\sigma_T \omega D^2 h_5 \tag{37}$$

Where S denotes the area of the rotating block *ABC*. The dimensionless functions h_1, h_2, h_3, h_4 and h_5 are given in Appendix C.

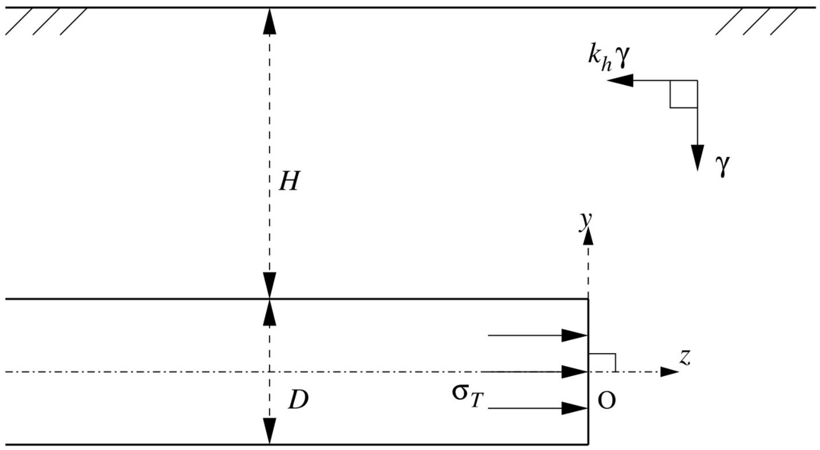

Figure 4. Plane strain stability analysis problem.

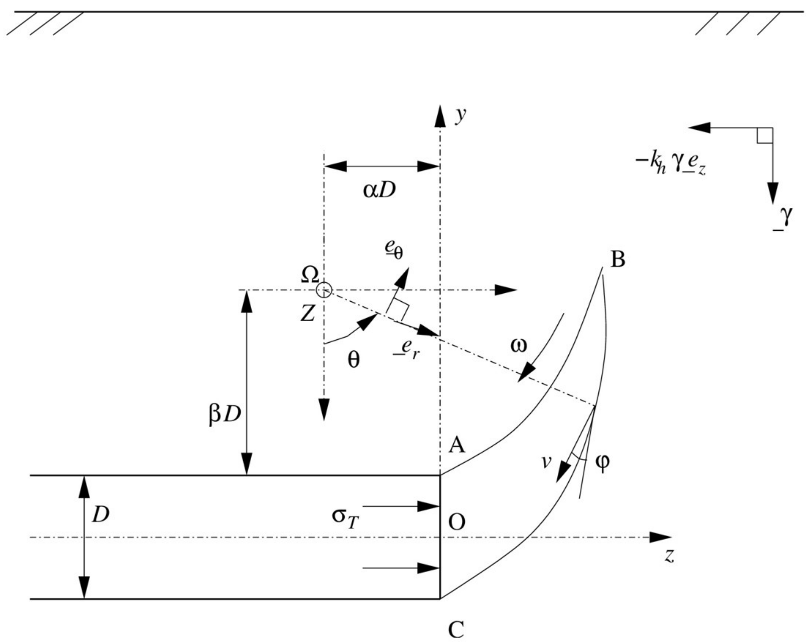

Figure 5. The 2D horn-like failure mechanism of Chambon & Corté (1990).

On the other hand, the expression of maximum resisting work rate is due to the contribution of velocity jump along the logarithmic spirals *AB* and *BC*. Hence,

$$P_{mr} = \int_{AB} \Pi\left(\underline{\upsilon},[\underline{U}]\right)dl + \int_{CB} \Pi\left(\underline{\upsilon},[\underline{U}]\right)dl = c\omega D^2\left(h_6 + h_7\right) \quad (38)$$

Where h_6 and h_7 are dimensionless functions given in the Appendix C.

Applying the fundamental inequality (2) to the considered failure mechanism yields:

$$\frac{\sigma_{T3}}{\gamma D} = \underbrace{\mathrm{Max}}_{(\theta_C,\theta_A)}\left[\left(\frac{h_1+h_2}{h_5} + k_h\frac{h_3+h_4}{h_5}\right) - \frac{c}{\gamma D}\frac{h_6+h_7}{h_5}\right] \le \frac{\sigma_T}{\gamma D} \quad (39)$$

The problem to be solved for obtaining the best lower bound $\frac{\sigma_{T3}}{\gamma D}$ consists in maximizing the function appearing in the left-side hand of above inequality with respect to the two angular parameters θ_C and θ_A, which must satisfy the following constraints:

$$0 < \theta_C < \theta_A < \frac{\pi}{2} \quad (40)$$

$$\theta_A < \theta_B = \frac{\theta_A + \theta_C}{2} + \frac{1}{2\tan(\varphi)} \mathrm{Ln}\left(\frac{\sin(\theta_A)}{\sin(\theta_C)}\right) < \frac{3\pi}{2} \quad (41)$$

5. Numerical results

In the preceding section, three failure mechanisms were analyzed in order to derive lower bound estimates for stabilizing value of the pressure σ_T applied to the tunnel face. In the following sections, we provide a comparison with previous results as well as a study of the effects of different relevant problem parameters on the limit face pressure value.

5.1 Comparison with previous results

Mollon et al. (2010) calculated a lower bound of the pressure σ_T applied to the tunnel face, based on kinematic approach of limit analysis. They used a 3D multiblock failure mechanism and compared their results to centrifuge experiments performed by Chambon & Corté (1994).

In this section, we compare the results obtained using the three failure mechanisms presented in this paper to the theoretical results of Mollon et al. (2010) and the experiments of Chambon & Corté (1994). Two experiments carried out by Chambon & Corté (1994) are considered for the comparisons. Furthermore, it should be noted that the failure mechanism was constructed using a numerical procedure by Mollon et al. (2010). However, in this paper, the failure mechanisms are analytically determined.

- First experiment

Table 1 presents the parameters of an experiment performed by Chambon & Corté (1994).

Four numerical simulations were performed by Mollon et al. (2010) in order to obtain theoretically the experimental results of Chambon & Corté (1994). These results are presented together with results provided by the three failure mechanisms considered in this paper in Table 2.

- Second experiment

Table 3 provides the parameters of an experiment performed by Chambon & Corté (1994).

Four numerical simulations were performed by Mollon et al. (2010) in order to obtain theoretically the experimental results of Chambon & Corté (1994). These results are presented together with results provided by the three failure mechanisms considered in this paper in Table 4.

The results presented by this paper are in good agreement with the results obtained by Mollon et al. (2010). Indeed, the horn mechanism provides a lower bound for σ_T which is very close to that obtained by Mollon et al. (2010) as clearly shown by Tables 2 and 4.

Moreover, the approach presented by this paper provides results close to the experiments of Chambon & Corté (1994).

On the other hand, the results obtained using the 2D mechanism of Chambon & Corté (1990) overestimate the upper bound of σ_T.

5.2 Comparison with finite element solutions

In order to study the accuracy of the lower bound calculated using the approach presented in this paper, the

Table 1. Centrifuge experiment performed by Chambon & Corté (1994).

c (kPa)	φ (°)	γ (kN/m³)	D (m)	$\frac{C}{D}$	σ_T (kPa)
0-5	38-42	16.1	5	2	4

Table 2. Lower bound of σ_T (kPa).

	σ_T Mollon et al. (2010) (kPa)	σ_{T1} cone mechanism (kPa)	σ_{T2} horn mechanism (kPa)	σ_{T3}, 2D mechanism of Chambon & Corté (1990) (kPa)
$c = 0$; $\varphi = 38°$	6.8	5.923	6.81	10.751
$c = 5$ kPa ; $\varphi = 38°$	0.4	stable	0.37	4.351
$c = 0$; $\varphi = 42°$	5.3	4.761	5.45	8.57
c=5 kPa ; φ =42°	stable	stable	stable	3.017

Table 3. Centrifuge experiment performed by Chambon & Corté (1994).

c (kPa)	φ (°)	γ (kN/m³)	D (m)	$\frac{C}{D}$	σ_T (kPa)
0-5	38-42	16.0	10	4	8.2

Table 4. Lower bound of σ_T (kPa).

	σ_T Mollon et al. (2010) (kPa)	σ_{T1} cone mechanism (kPa)	σ_{T2} horn mechanism (kPa)	σ_{T3}, 2D mechanism of Chambon & Corté (1990) (kPa)
c=0; φ = 38°	13.6	11.772	13.53	21.368
c=5 kPa; φ = 38°	7.1	5.373	7.09	14.968
c=0; φ = 42°	10.5	9.463	10.82	17.034
c=5 kPa ; φ = 42°	5	3.91	5.22	11.481

Table 5. Lower and upper bounds of σ_T (kPa).

	σ_{T1}, cone mechanism (kPa)	σ_{T2}, horn mechanism (kPa)	σ_{T3}, 2D mechanism of Chambon & Corté (1990) (kPa)	σ_T, kinematic approach OptumG2 (kPa)	σ_T, static approach OptumG2 (kPa)
c = 0; φ = 38°	11.772	13.53	21.368	20.38	23.12
c = 5 kPa; φ = 38°	5.373	7.09	14.968	13.98	16.759
c = 0; φ = 42°	9.463	10.82	17.034	15.836	18.24
c = 5 kPa; φ = 42°	3.91	5.22	11.481	10.284	12.684

results obtained are compared to the finite element solutions provided by the OptumG2 software. This software implements a finite element formulation of the static and kinematic approaches relating to limit analysis theory.

In order to compare the results, the parameters presented in Table 3 were considered for the numerical simulations. The results of the comparisons are shown in Table 5.

It is recalled that the static approach of the limit analysis provides an upper bound of the pressure σ_T. Moreover, the kinematic approach of the limit analysis provides a lower bound of the pressure σ_T. These two approaches are considered by the OptumG2 software in order to obtain a lower bound and an upper bound of the pressure σ_T necessary for the stability of the tunnel face. When the two bounds have close values, this allows to evaluate the real value of the pressure σ_T. For this reason, Table 5 provides the values calculated by the two approaches of limit analysis.

In addition, it is emphasized that the OptumG2 software enables the study of two-dimensional problems. The simulations carried out using the OptumG2 software are considered to make comparisons with the results obtained by the 3 failure mechanisms presented in this paper. In addition, the considered problem will be investigated with a 3D finite element software. It is a perspective of the work presented in this paper.

The static and kinematic approaches carried out using the OptumG2 software start from an initial discretization of the geometry of the problem studied. Thereafter, the software carries out an automatic refinement of the mesh. For example, Figure 6 shows the optimized finite element mesh resulting from the kinematic approach of the limit analysis by considering the parameters: c = 0 kPa and φ = 38°.

It should be noted that the optimized mesh consists of 898 triangular elements. The time needed to do the calculations is 5 seconds on a standard personal computer.

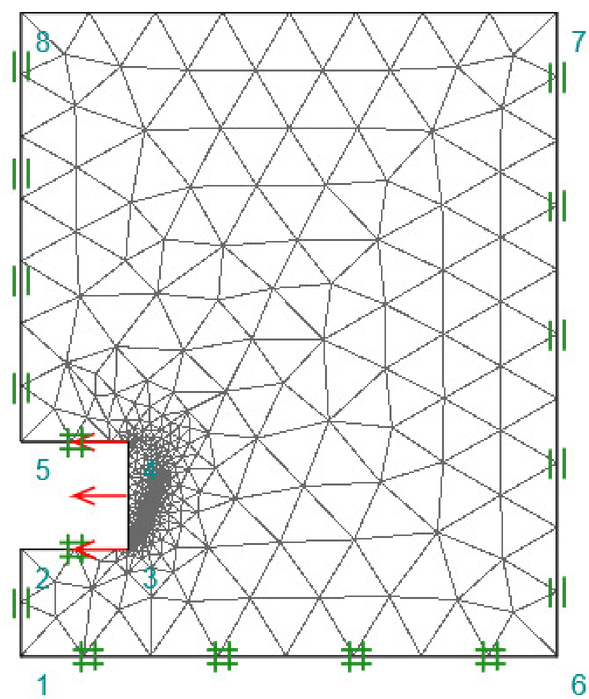

Figure 6. Optimized finite element mesh obtained from kinematic approach of limit analysis using optumG2 software.

Moreover, Figure 7 indicates the velocity field resulting from the kinematic approach by finite elements.

First, we note that the OptumG2 software provides a local failure mechanism (Figure 7) which agrees with the experimental results of Chambon & Corté (1994).

Moreover, the results of the kinematic approach of OptumG2 are very close to those obtained using the 2D

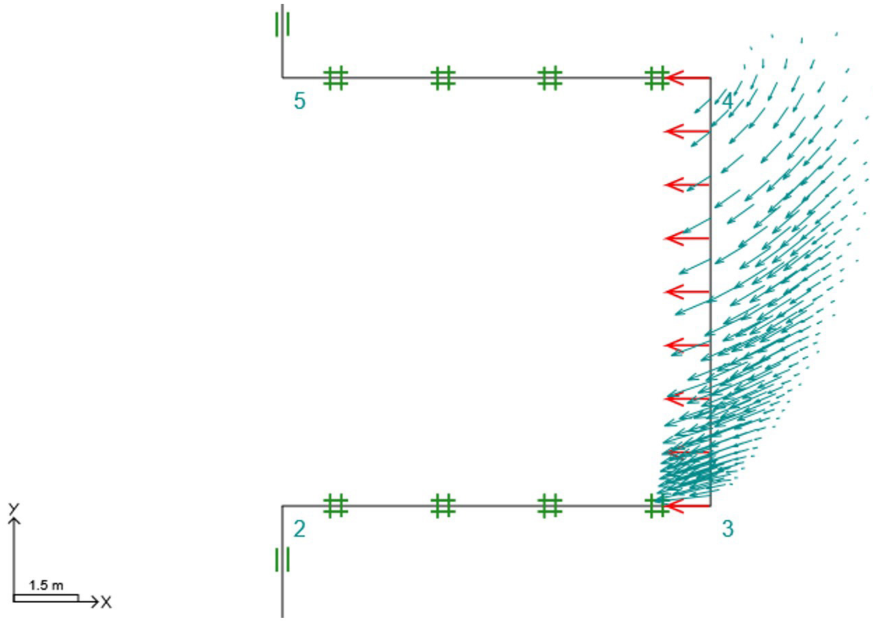

Figure 7. Optimal velocity field obtained using OptumG2 software.

mechanism of Chambon & Corté (1990). This result can be explained by the fact that the OptumG2 software and the 2D mechanism of Chambon & Corté (1990) both solve a two-dimensional problem.

Furthermore, it is emphasized that the 2D approach is used to carry out a rapid study which allows to have a first idea concerning the value of the stress σ_T to be applied to the tunnel face. This study is very useful and very easy to carry out. However, the tunnel construction problem is a three-dimensional problem. Therefore, after the 2D study, it is necessary to carry out a 3D study which is more complicated than the 2D study, but which provides more precise results.

Finally, if we compare the relative error between the results obtained by considering the 3D horn mechanism and those obtained using the 2D mechanism of Chambon & Corté (1990) (results presented in table 5), we see that this relative error is between 57% and 120% $\left(\text{relative error} = \left(\sigma_{T3} - \sigma_{T2}\right)/\sigma_{T2}\right)$.

5.3 Effects of non-dimensional parameter $c/(\gamma D)$

In the preceding sections, comparisons were carried out in order to study the precision of the results provided by the approach presented in this paper. In this section, the parametric study carried out makes it possible to compare the performances of the 3 failure mechanisms which are considered in this paper.

In order to study the effect of the non-dimensional parameter $c/(\gamma D)$ on the normalized pressure $\sigma_T/(\gamma D)$, numerical simulations were carried out considering the following parameters: φ = 40° and k_h = 0.1. The results obtained using the 3 failure mechanisms are shown in Figure 8. The normalized pressure $\sigma_T/(\gamma D)$ is a decreasing function of the non-dimensional parameter $c/(\gamma D)$. Moreover, the horn mechanism provides the best lower bound of $\sigma_T/(\gamma D)$.

Moreover, the 2D mechanism of Chambon & Corté (1990), overestimates the lower bound of $\sigma_T/(\gamma D)$.

Finally, it should be noted that:

$$\frac{\dfrac{\sigma_{T2}}{\gamma D}\left(\dfrac{c}{\gamma D}=0\right)}{\dfrac{\sigma_{T2}}{\gamma D}\left(\dfrac{c}{\gamma D}=0.0556\right)} = 4.437 \qquad (42)$$

The previous equation shows the significant effect of the value of $c/(\;\;D)$ on the value of $\sigma_{T2}/(\gamma D)$.

5.4 Effects of the friction angle φ

In order to study the effect of the friction angle φ on the normalized pressure $\sigma_T/(\gamma D)$, numerical simulations were carried out considering the following parameters: $\gamma = 18$ kN/m^3, c = 0 kPa, D = 10 m, k_h = 0.1 and $\varphi \in [30°, 45°]$. It should be noted that $k_h = 0.1$ is a reasonable value for the horizontal seismic coefficient which has values between 0 and 0.4.

The results obtained using the 3 failure mechanisms are shown in Figure 9. The normalized pressure $\sigma_T/(\gamma D)$ is a decreasing function of the friction angle φ. Moreover, the horn mechanism provides the best lower bound of $\sigma_T/(\gamma D)$. In addition, the 2D mechanism of Chambon & Corté (1990) overestimates the lower bound of $\sigma_T/(\gamma D)$.

Finally, it should be noted that:

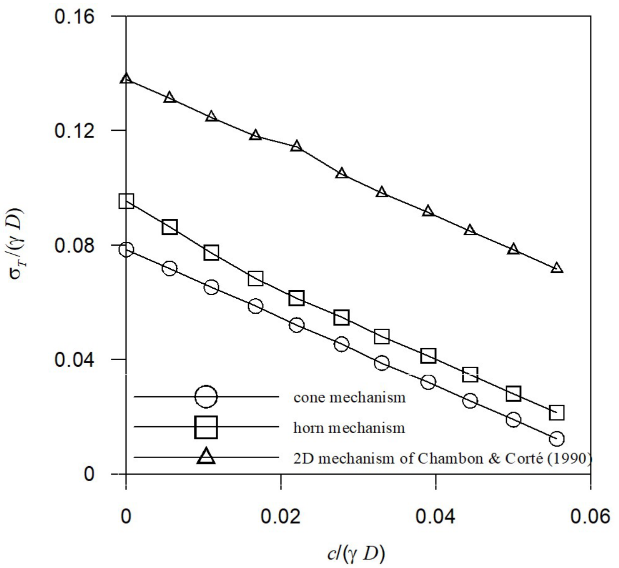

Figure 8. Effects of non-dimensional parameter $c/(\gamma D)$ on the normalized pressure $\sigma_T/(\gamma D)$.

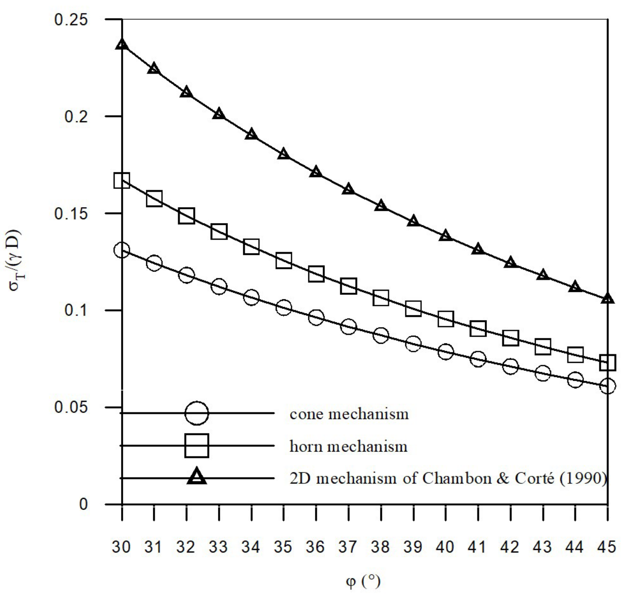

Figure 9. Effects of the friction angle φ on the normalized pressure $\sigma_T/(\gamma D)$.

$$\frac{\frac{\sigma_{T2}}{\gamma D}\left(\varphi = 30°\right)}{\frac{\sigma_{T2}}{\gamma D}\left(\varphi = 45°\right)} = 2.288 \tag{43}$$

The previous equation shows the significant effect of the value of the friction angle φ on the value of $\sigma_{T2}/(\gamma D)$.

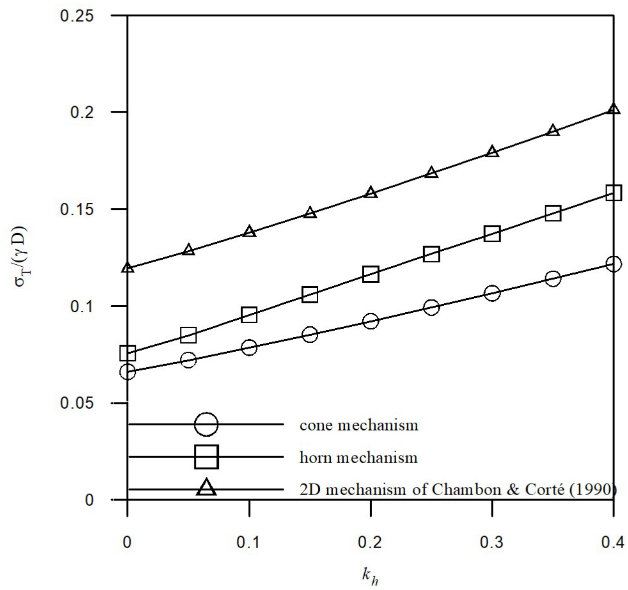

Figure 10. Effects of the horizontal seismic coefficient k_h on the normalized pressure $\sigma_T/\gamma D$.

5.5 Earthquake effects

In order to study the effect of the horizontal seismic coefficient k_h on the normalized pressure $\sigma_T/(\gamma D)$, numerical simulations were carried out considering the following parameters: $\gamma = 18$ kN/m^3, $c = 0$ kPa, $D = 10$ m and $\varphi = 40°$. The results obtained using the 3 failure mechanisms are shown in Figure 10. The normalized pressure $\sigma_T/(\gamma D)$ is an increasing function of the horizontal seismic coefficient k_h. Moreover, the horn mechanism provides the best lower bound of $\sigma_T/(\gamma D)$. Finally, the 2D mechanism of Chambon & Corté (1990) overestimates the lower bound of $\sigma_T/(\gamma D)$.

6. Conclusion

In this paper, the pressure applied to the tunnel face in order to stabilize it was calculated. The soil resistance is assumed to follow the Mohr-Coulomb failure criterion. The kinematic approach of limit analysis was used in order to calculate a lower bound of the pressure σ_T applied to the tunnel face. The better lower bound was calculated after maximizing the objective function with respect to the parameters of the failure mechanism. Three mechanisms were considered in order to calculate the lower bound of σ_T: cone mechanism, horn mechanism and 2D mechanism of Chambon & Corté (1990). This approach provided original analytical expressions allowing the evaluation of the pressure stabilizing the tunnel face.

Comparisons were made between the results of the approach presented in this paper with the experimental and theoretical results of the bibliography and showed good agreement.

Other comparisons were made between the 2 three-dimensional mechanisms (cone mechanism and horn mechanism) with the two-dimensional mechanism of Chambon & Corté (1990) and the numerical results obtained using the OptumG2 software. It has been shown that the 2D and 3D approaches provide relatively close results.

Moreover, a numerical study was performed in order to assess the influence of the involved parameters on the value of the lower bound of the pressure σ_T. It was remarked that the lower bound estimate of σ_T is an increasing function of the horizontal seismic coefficient k_h. Furthermore, it is a decreasing function of dimensionless parameter $c/(\gamma D)$ and the friction angle φ.

Acknowledgements

The authors are very grateful to Optum Computational Engineering (Optumce) for providing an academic license of OptumG2 software.

Declaration of interest

The authors have no conflicts of interest to declare. All co-authors have observed and affirmed the contents of the paper and there is no financial interest to report.

Authors' contributions

Zied Saada: methodology, writing original draft, investigation, discussion of results, writing programs of all calculations, validation. Denis Garnier: methodology, validation, discussion of results, review and editing. Samir Maghous: methodology, validation, discussion of results, review and editing.

Data availability

The datasets generated during and/or analyzed during the current study are available from the corresponding author on reasonable request.

Declaration of use of generative artificial intelligence

No generative artificial intelligence (GenAI) assistance tools were used in writing this paper.

List of symbols and abbreviations

$a = D/2$	tunnel radius
b	distance defining the ellipse of intersection of the cone and the tunnel face (Figure 2)
c	cohesion
$\underline{\underline{d}}$	strain rate tensor
d_1, d_2, d_3	Eigenvalues of $\underline{\underline{d}}$
e_i	Unit vectors related to coordinates
f, f_i, f_i'	Dimensionless functions
k_h	Horizontal seismic acceleration
r	First coordinate of the cylindrical coordinate system.
$\underline{v}$	Velocity of translation of the cone
x, y, z	Coordinates
A-lateral	Lateral surface of the cone
D	Tunnel diameter
2D, 3D	Two- and three-dimensional
$F\left(\underline{\underline{\sigma}}\right)$	Function that defines the Mohr-Coulomb failure criterion
H	Depth of cover of the tunnel
J	Lateral surface of the horn
P_{ext}	Work rate of external loads
P_{mr}	Rate of maximum resisting work
P_γ	Work rate of the soil weight
P_{k_h}	Work rate of the seismic acceleration
P_{σ_T}	Work rate of face pressure
$\underline{U}$	Admissible velocity field
$[\underline{U}]$	Jump of velocity
V-cone	Volume of the translational conical block
X, Y, Z	Coordinates
α	Angle between the cone axis and the tunnel axis (for cone mechanism) and a positive scalar defined in Figure 3 (for horn mechanism).
γ	Soil unit weight
φ	Friction angle
$\underline{\nu}$	Normal unit vector to a surface
ω	Angular velocity
σ_T, σ_{Ti}	Tunnel face pressure
$\sigma_1, \sigma_2, \sigma_3$	Principal stresses
$\underline{\underline{\sigma}}$	Stress tensor
θ	Second coordinate of the cylindrical coordinate system
Ω	Soil volume
Π	Support functions defined by equations (4) and (5)
Σ	Intersection between the tunnel face and the cone volume (for cone mechanism) or the horn volume (for horn mechanism)

References

Askoy, C.O., & Onargan, T. (2010). The role of umbrella arch and face bolt as deformation preventing support system in preventing building damages. *Tunnelling and Underground Space Technology*, 25, 553-559.

Broms, B.B., & Bennermark, H. (1967). Stability of clay at vertical openings. *Journal of the Soil Mechanics and Foundations Division*, 93(SM1), 71-94.

Chambon, P., & Corté, J.F. (1989). Stabilité du front de taille d'un tunnel faiblement enterré: Modélisation en centrifugeuse. In *Proceedings, Colloquium Tunnels et*

Micro-tunnels en terrains meubles, Paris, France (pp. 307-315). Ecole Nationale des Ponts et Chaussèes Press. (in French).

Chambon, P., & Corté, J.F. (1990). Stabilité du front de taille d'un tunnel dans un milieu frottant, approche cinématique en calcul à la rupture. *Revue Française de Géotechnique*, 51, 51-59. [in French]

Chambon, P., & Corté, J.F. (1994). Shallow tunnels in cohesionless soil: stability of tunnel face. *Journal of Geotechnical Engineering*, 120(7), 1148-1165.

Chen, G.H., Zou, J.F., & Qian, Z.H. (2022). Analysis of tunnel face stability with non-linear failure criterion under the pore water pressure. *European Journal of Environmental and Civil Engineering*, 26(7), 2950-2962.

Chen, X., Zhang, K., & Wang, W. (2023). Seismic stability analysis of tunnel faces in heterogeneous and anisotropic soils using modified pseudodynamic method. *Sustainability*, 15(14), 11083.

Cheng, H., Chen, J., Chen, R., Huang, J., & Li, J. (2019). Three-dimensional analysis of tunnel face stability in spatially variable soils. *Computers and Geotechnics*, 111, 76-88.

Cuvillier, A. (2001). *Aspects mécaniques du creusement d'un tunnel en milieu poreux saturé* [Doctoral thesis]. Ecole Nationale des Ponts et Chaussées.

Davis, E.H., Gunn, M.J., Mair, R.J., & Seneviratne, H.N. (1980). The stability of shallow tunnels and underground openings in cohesive material. *Geotechnique*, 30(4), 397-416.

De Buhan, P., Cuvillier, A., Dormieux, L., & Maghous, S. (1999). Face stability of shallow circular tunnels driven under the water table: a numerical analysis. *International Journal for Numerical and Analytical Methods in Geomechanics*, 23, 79-95.

Dormieux, L., & Leca, E. (1993). Stabilité du front de taille d'un tunnel dans un milieu sans résistance à la traction. In *Geotechnical Engineering of Hard Soils - Soft Rocks* (pp. 1409-1415).Rotterdam: Balkema. (in French).

Funatsu, T., Hoshino, T., Sawae, H., & Shimizu, N. (2008). Numerical analysis to better understand the mechanism of the effects of ground supports and reinforcements on the stability of tunnels using the distinct element method. *Tunnelling and Underground Space Technology*, 23, 561-573.

Hisatake, M., Ohno, S., Katayama, T., Ohmae, Y., & Sano, S. (2009). Effects of the ring-cut excavation method on the restraint of displacements ahead of a tunnel face. *Tunnelling and Underground Space Technology*, 24, 547-554.

Hou, C.T., & Yang, X.L. (2020). Seismic stability of 3D tunnel face considering tensile strength cut-off. *KSCE Journal of Civil Engineering*, 24(7), 2232-2243.

Huang, F., Ou, R., Li, Z., Yang, X.L., & Ling, T. (2018). Limit analysis for the face stability of a shallow-shield tunnel based on a variational approach to the blow-out failure mode. *International Journal of Geomechanics*, 18(6), 04018038.

Juneja, A., Hegde, A., Lee, F.H., & Yeo, C.H. (2010). Centrifuge modelling of tunnel face reinforcement using forepoling. *Tunnelling and Underground Space Technology*, 25, 377-381.

Kamata, H., & Mashimo, H. (2003). Centrifuge model test of tunnel face reinforcement by bolting. *Tunnelling and Underground Space Technology*, 18, 205-212.

Leca, E., & Dormieux, L. (1990). Upper and lower bound solutions for the face stability of shallow circular tunnels in frictional material. *Geotechnique*, 40(4), 581-606.

Leca, E., & Dormieux, L. (1992). Contribution à l'étude de la stabilité du front de taille d'un tunnel en milieu cohérent. *Revue Française de Géotechnique*, 61, 5-16. [in French]

Lee, I.M., Nam, S.W., & Ahn, J.H. (2003). Effect of seepage forces on tunnel face stability. *Canadian Geotechnical Journal*, 40, 342-350.

Lee, Y.Z., & Shubert, W. (2008). Determination of the round length for tunnel excavation in weak rock. *Tunnelling and Underground Space Technology*, 23, 221-231.

Li, T.Z., & Yang, X.L. (2019). Three-dimensional face stability of shallow-burried tunnels with tensile strength cut-off. *Computers and Geotechnics*, 110, 82-93.

Man, J., Zhou, M., Zhang, D., Huang, H., & Chen, J. (2022). Face stability analysis of circular tunnels in layered rock masses using the upper bound theorem. *Journal of Rock Mechanics and Geotechnical Engineering*, 14, 1836-1848.

Mollon, G., Dias, D., & Soubra, A. (2010). Face stability analysis of circular tunnels driven by a pressurized shield. *Journal of Geotechnical and Geoenvironmental Engineering*, 136(1), 215-229.

Mollon, G., Dias, D., & Soubra, A.H. (2013). Continuous velocity fields for collapse and blowout of a pressurized tunnel face in purely cohesive soil. *International Journal for Numerical and Analytical Methods in Geomechanics*, 37(13), 2061-2083.

Pan, Q., & Dias, D. (2018). Three dimensional face stability of a tunnel in weak rock masses subjected to seepage forces. *Tunnelling and Underground Space Technology*, 71, 555-566.

Paternesi, A., Schweiger, H.F., & Scarpelli, G. (2017). Numerical analyses of stability and deformation behavior of reinforced and unreinforced tunnel faces. *Computers and Geotechnics*, 88, 256-266.

Pellet, F., Descoeudres, F., & Egger, P. (1993). The effect of water seepage forces on the face stability of an experimental microtunnel. *Canadian Geotechnical Journal*, 30, 363-369.

Saada, Z., Maghous, S., & Garnier, D. (2013). Pseudo-static analysis of tunnel face stability using the generalized Hoek-Brown strength criterion. *International Journal for Numerical and Analytical Methods in Geomechanics*, 37, 3194-3212.

Salençon, J. (1983). *Calcul à la rupture et analyse limite*. France: Ecole Nationale des Ponts et Chaussèes Press. (in French).

Salençon, J. (1990). An introduction to the yield design theory and its applications to soil mechanics. *European Journal of Mechanics. A, Solids*, 9(5), 477-500.

Schofield, A.N. (1980). Cambridge geotechnical centrifuge operations. *Geotechnique*, 30(3), 227-288.

Seed, H.B. (1979). Considerations in the earthquake-resistant design of earth and rockfill dams. *Geotechnique*, 29(3), 215-263.

Shin, J.H., Choi, Y.K., Kwon, O.Y., & Lee, S.D. (2008). Model testing for pipe-reinforced tunnel heading in a granular soil. *Tunnelling and Underground Space Technology*, 23, 241-250.

Tschuchnigg, F., Schweiger, H.F., Sloan, S.W., Lyamin, A.V., & Raissakis, I. (2015). Comparison of finite element limit analysis and strength reduction techniques. *Geotechnique*, 65(4), 249-257.

Xu, J.S., Du, D.C., & Yang, Z.H. (2015). Upper bound analysis for deep tunnel face with joined failure mechanism of translation and rotation. *Journal of Central South University*, 22(11), 4310-4317.

Yang, X.L., Yoo, C., & Zhang, J.H. (2016). Safe retaining pressures for pressurized tunnel face using nonlinear failure criterion and reliability theory. *Journal of Central South University*, 23(3), 708-720.

Zhang, B., Ma, Z., Wang, X., Zhang, J., & Peng, W. (2020). Reliability analysis of anti-seismic stability of 3d pressurized tunnel faces by response surfaces method. *Geomechanics and Engineering*, 20(1), 43-54.

Zhang, B., Wang, X., Zhang, J.S., & Meng, F. (2017). Three-dimensional limit analysis of seismic stability of tunnel faces with quasi-static methods. *Geomechanics and Engineering*, 13(2), 301-318.

Zhang, C., Han, K., & Zhang, D. (2015). Face stability analysis of shallow circular tunnels in cohesive-frictional soils. *Tunnelling and Underground Space Technology*, 50, 345-357.

Zhang, D., Sun, W., Wang, C., & Yu, B. (2021). Reliability analysis of seismic stability of shield tunnel face under multiple correlated failure modes. *KSCE Journal of Civil Engineering*, 25(8), 3172-3185.

Zhang, J.H., Wang, W.J., Zhang, B., Zhang, D.B., & Song, J.C. (2019b). Upper bound solution for required supporting pressure applied on a deep shield tunnel face under different ground water levels. *Geotechnical and Geological Engineering*, 37(1), 491-499.

Zhang, Z., Li, H., Yang, H., & Wang, B. (2019a). Failure modes and face instability of shallow tunnels under soft grounds. *International Journal of Damage Mechanics*, 28(4), 566-589.

Zhang, Z., Shi, X., Wang, B., & Li, H. (2018). Stability of NATM tunnel faces in soft surrounding rocks. *Computers and Geotechnics*, 96, 90-102.

Zhao, L., Li, D., Li, L., Yang, F., Cheng, X., & Luo, W. (2017). Three-dimensional stability analysis of a longitudinally inclined shallow tunnel face. *Computers and Geotechnics*, 87, 32-48.

Zhong, J.H., & Yang, X.L. (2020). Kinematic analysis of the three-dimensional stability for tunnel faces by pseudodynamic approach. *Computers and Geotechnics*, 128, 103802.

Zou, J., Chen, G., & Qian, Z. (2019). Tunnel face stability in cohesion-frictional soils considering the soil arching effect by improved failure models. *Computers and Geotechnics*, 106, 1-17.

Appendix A. Translational cone failure mechanism

Some geometrical quantities should be obtained in order to derive the work rate of external loads and the maximum resisting work rate.
In this study, two axis systems are used: (Ω, X, Y, Z) that is associated with the cone, and (O, x, y, z) which is associated with the tunnel. The transformation between both coordinate systems are allowed by the equations below:

$$X = x \tag{A1}$$

$$Y = \frac{D}{2}\sin(\alpha)\tan(\varphi) - y\cos(\alpha) + z\sin(\alpha) \tag{A2}$$

$$Z = \frac{D}{2}\frac{\cos(\alpha)}{\tan(\varphi)} - y\sin(\alpha) - z\cos(\alpha) \tag{A3}$$

The cone under consideration is characterized, with respect to coordinate system (Ω, X, Y, Z), by the following equation

$$X^2 + Y^2 = Z^2\tan^2(\varphi) \tag{A4}$$

The intersection between the tunnel face and the cone is an ellipse for which semi-axis are given by

$$a = \frac{D}{2} \tag{A5}$$

$$b = \frac{D}{2}\frac{\sqrt{\cos(\alpha+\varphi)\cos(\alpha-\varphi)}}{\cos(\varphi)} \tag{A6}$$

The area A-base of the cone base is expressed as

$$A - base = \frac{\pi}{4}D^2\frac{\sqrt{\cos(\alpha+\varphi)\cos(\alpha-\varphi)}}{\cos(\varphi)} \tag{A7}$$

The volume of the cone is equal to

$$V - cone = \frac{\pi}{12}D^3\frac{\left[\cos(\alpha+\varphi)\cos(\alpha-\varphi)\right]^{\frac{3}{2}}}{\cos(\varphi)\sin(2\varphi)} \tag{A8}$$

The lateral area of the cone is given by

$$A - lateral = \frac{\pi}{4}D^2\cos(\alpha)\frac{\left[\cos(\alpha+\varphi)\cos(\alpha-\varphi)\right]^{\frac{1}{2}}}{\sin(\varphi)\cos(\varphi)} \tag{A9}$$

Non dimensional functions f_1, f_1', f_2 and f_3 are given by

$$f_1 = \frac{\pi}{12}\sin(\alpha)\frac{\left[\cos(\alpha+\varphi)\cos(\alpha-\varphi)\right]^{\frac{3}{2}}}{\cos(\varphi)\sin(2\varphi)} \tag{A10}$$

$$f_1' = \frac{\pi}{12}\cos(\alpha)\frac{\left[\cos(\alpha+\varphi)\cos(\alpha-\varphi)\right]^{\frac{3}{2}}}{\cos(\varphi)\sin(2\varphi)} \tag{A11}$$

$$f_2 = \frac{\pi}{4}\frac{\cos(\alpha)}{\cos(\varphi)}\sqrt{\cos(\alpha+\varphi)\cos(\alpha-\varphi)} \tag{A12}$$

$$f = \frac{\pi}{4}\frac{\cos(\alpha)}{\sin(\varphi)}\sqrt{\cos(\alpha+\varphi)\cos(\alpha-\varphi)} \tag{A13}$$

Appendix B. 3D rotational horn failure mechanism

The maximum resisting work rate is given by

$$P_{mr} = \int\int_{J} \Pi\left(\underline{\upsilon},[\underline{v}]\right) d\Sigma = \int\int_{S_{J1}} \Pi\left(\underline{\upsilon},[\underline{v}]\right) d\Sigma + \int\int_{S_{J2}} \Pi\left(\underline{\upsilon},[\underline{v}]\right) d\Sigma \quad \text{(B1)}$$

The plane $\left(\Omega, \underline{\Omega A}, \underline{e}_Z\right)$ divide the lateral surface of the horn into two parts: S_{J1} the surface that contains point B and S_{J2} the surface that contains point C.
In addition, the Π-function is expressed as

$$\Pi\left(\underline{\upsilon},[\underline{v}]\right) = c\cos(\varphi)V = c\cos(\varphi)\omega r \quad \text{(B2)}$$

The two integrals written above are given by the following equations

$$\int\int_{S_{J1}} \Pi\left(\underline{\upsilon},[\underline{v}]\right) d\Sigma = c\omega D^3 \cos(\varphi) \times \int_{\theta=\theta_A}^{\theta_B} \int_{t=-\pi}^{\pi} g\left[f + g\cos(t)\right] \begin{bmatrix} \left[f + g\cos(t)\right]^2 + \\ \tan^2(\varphi)\left[g + f\cos(t)\right]^2 + \\ f^2 \tan^2(\varphi)\sin^2(t) \end{bmatrix}^{\frac{1}{2}} dt d\theta \quad \text{(B3)}$$

$$\int\int_{S_{J2}} \Pi\left(\underline{\upsilon},[\underline{v}]\right) d\Sigma = c\omega D^3 \cos(\varphi) \times \int_{\theta=\theta_C}^{\theta_A} \int_{t=-t_0(\theta)}^{t_0(\theta)} g\left[f + g\cos(t)\right] \begin{bmatrix} \left[f + g\cos(t)\right]^2 + \\ \tan^2(\varphi)\left[g + f\cos(t)\right]^2 + \\ f^2 \tan^2(\varphi)\sin^2(t) \end{bmatrix}^{\frac{1}{2}} dt d\theta \quad \text{(B4)}$$

In which function t_0 is expressed as

$$t_0(\theta) = \arccos\left(\frac{\dfrac{\alpha}{\sin(\theta)} - f(\theta)}{g(\theta)}\right) \quad \text{(B5)}$$

The non dimensional functions g_1 and g_2 are introduced in order to simplify the expressions of the two integrals given below:

$$\int\int_{S_{J1}} \Pi\left(\underline{\upsilon},[\underline{v}]\right) d\Sigma = c\omega D^3 g_1 \quad \text{(B6)}$$

$$\int\int_{S_{J2}} \Pi\left(\underline{\upsilon},[\underline{v}]\right) d\Sigma = c\omega D^3 g_2 \quad \text{(B7)}$$

These two integrals are numerically calculated.
The work rate due to the unit weight of the soil is expressed as

$$P_\gamma = \int\int\int_{V_{J1}} \left(-\gamma \underline{e}_y\right).\left(-\omega r \underline{e}_\theta\right) dV + \int\int\int_{V_{J2}} \left(-\gamma \underline{e}_y\right).\left(-\omega r \underline{e}_\theta\right) dV \quad \text{(B8)}$$

The plane $\left(\Omega, \underline{\Omega A}, \underline{e}_Z\right)$ divide the volume of the horn into two parts: V_{J1} the volume that contains point B and V_{J2} the volume that contains point C.
The first integral is expressed as:

$$\iiint_{V_{J1}} \left(-\gamma \underline{e}_y\right).\left(-\omega r \underline{e}_\theta\right) dV = \gamma \omega D^4 g_3 \quad \text{(B9)}$$

$$g_3 = \frac{\pi}{16}\left(g_{31} + g_{32} + g_{33} + g_{34} + g_{35}\right) \quad \text{(B10)}$$

Non-dimensional functions g_{31}, g_{32}, g_{33}, g_{34} and g_{35} are given by

$$g_{31} = -\frac{5}{4}\frac{\left(\alpha^2 + (1+\beta)^2\right)^2}{16\tan^2(\varphi)+1} e^{4\tan(\varphi)\theta_C} \times \\ \left(\begin{array}{l} e^{-4\tan(\varphi)\theta_B}\left(\cos(\theta_B) + 4\tan(\varphi)\sin(\theta_B)\right) - e^{-4\tan(\varphi)\theta_A} \\ \left(\cos(\theta_A) + 4\tan(\varphi)\sin(\theta_A)\right) \end{array}\right) \quad \text{(B11)}$$

$$g_{32} = \frac{\left(\alpha^2 + (1+\beta)^2\right)^{\frac{3}{2}}\left(\alpha^2+\beta^2\right)^{\frac{1}{2}}}{4\tan^2(\varphi)+1} e^{\tan(\varphi)\left(-\theta_A + 3\theta_C\right)} \times \\ \left(e^{-2\tan(\varphi)\theta_B}\left(\cos(\theta_B) + 2\tan(\varphi)\sin(\theta_B)\right) - e^{-2\tan(\varphi)\theta_A}\left(\cos(\theta_A) + 2\tan(\varphi)\sin(\theta_A)\right)\right) \quad \text{(B12)}$$

$$g_{33} = \frac{1}{2}\left(\alpha^2 + (1+\beta)^2\right)\left(\alpha^2+\beta^2\right) e^{\tan(\varphi)\left(2\theta_C - 2\theta_A\right)}\left(\cos(\theta_B) - \cos(\theta_A)\right) \quad \text{(B13)}$$

$$g_{34} = -\frac{\left(\alpha^2 + (1+\beta)^2\right)^{\frac{1}{2}}\left(\alpha^2+\beta^2\right)^{\frac{3}{2}}}{4\tan^2(\varphi)+1} e^{\tan(\varphi)\left(\theta_C - 3\theta_A\right)} \times \\ \left(e^{2\tan(\varphi)\theta_B}\left(-\cos(\theta_B) + 2\tan(\varphi)\sin(\theta_B)\right) - e^{2\tan(\varphi)\theta_A}\left(-\cos(\theta_A) + 2\tan(\varphi)\sin(\theta_A)\right)\right) \quad \text{(B14)}$$

$$g_{35} = \frac{5}{4}\frac{\left(\alpha^2+\beta^2\right)^2}{16\tan^2(\varphi)+1} e^{-4\tan(\varphi)\theta_A} \times \\ \left(e^{4\tan(\varphi)\theta_B}\left(-\cos(\theta_B) + 4\tan(\varphi)\sin(\theta_B)\right) - e^{4\tan(\varphi)\theta_A}\left(-\cos(\theta_A) + 4\tan(\varphi)\sin(\theta_A)\right)\right) \quad \text{(B15)}$$

The second integral that appears in the work rate of unit weight writes

$$\iiint_{V_{J2}} \left(-\gamma \underline{e}_y\right).\left(-\omega r \underline{e}_\theta\right) dV = \gamma \omega D^4 g_4 \quad \text{(B16)}$$

Non dimensional function g_4 is expressed as

$$g_4 = 2\int_{\theta=\theta_C}^{\theta_A} g^2 \sin(\theta)\left[\frac{f^2}{2}\left[t_0 - \cos(t_0)\sin(t_0)\right] + \frac{2}{3} f\, g \sin^3(t_0) + \frac{g^2}{8}\left(t_0 - \frac{\sin(4t_0)}{4}\right)\right] d\theta \qquad \text{(B17)}$$

The integral given above is numerically calculated.
The work rate of seismic acceleration is expressed as

$$P_{k_h\gamma} = \iiint_{V_{J1}} \left(-k_h\gamma \underline{e}_z\right).\left(-\omega r \underline{e}_\theta\right) dV + \iiint_{V_{J2}} \left(-k_h\gamma \underline{e}_z\right).\left(-\omega r \underline{e}_\theta\right) dV \qquad \text{(B18)}$$

The first integral that appears in the equation above is given by

$$\iiint_{V_{J1}} \left(-k_h\gamma \underline{e}_z\right).\left(-\omega r \underline{e}_\theta\right) dV = k_h \gamma \omega D^4 g_3' \qquad \text{(B19)}$$

$$g_3' = \frac{\pi}{16}\left(g_{31}' + g_{32}' + g_{33}' + g_{34}' + g_{35}'\right) \qquad \text{(B20)}$$

Non-dimensional functions g_{31}', g_{32}', g_{33}', g_{34}' and g_{35}' are given by

$$g_{31}' = \frac{5}{4}\frac{\left(\alpha^2 + (1+\beta)^2\right)^2}{16\tan^2(\varphi)+1} e^{4\tan(\varphi)\theta_C} \times \qquad \text{(B21)}$$
$$\left(e^{-4\tan(\varphi)\theta_B}\left(-4\tan(\varphi)\cos(\theta_B) + \sin(\theta_B)\right) - e^{-4\tan(\varphi)\theta_A}\left(-4\tan(\varphi)\cos(\theta_A) + \sin(\theta_A)\right)\right)$$

$$g_{32}' = -\frac{\left(\alpha^2 + (1+\beta)^2\right)^{\frac{3}{2}}\left(\alpha^2 + \beta^2\right)^{\frac{1}{2}}}{4\tan^2(\varphi)+1} e^{\tan(\varphi)\left(-\theta_A + 3\theta_C\right)} \times \qquad \text{(B22)}$$
$$\left(e^{-2\tan(\varphi)\theta_B}\left(-2\tan(\varphi)\cos(\theta_B) + \sin(\theta_B)\right) - e^{-2\tan(\varphi)\theta_A}\left(-2\tan(\varphi)\cos(\theta_A) + \sin(\theta_A)\right)\right)$$

$$g_{33}' = -\frac{1}{2}\left(\alpha^2 + (1+\beta)^2\right)\left(\alpha^2 + \beta^2\right) e^{\tan(\varphi)\left(2\theta_C - 2\theta_A\right)}\left(\sin(\theta_B) - \sin(\theta_A)\right) \qquad \text{(B23)}$$

$$g_{34}' = -\frac{\left(\alpha^2 + (1+\beta)^2\right)^{\frac{1}{2}}\left(\alpha^2 + \beta^2\right)^{\frac{3}{2}}}{4\tan^2(\varphi)+1} e^{\tan(\varphi)\left(\theta_C - 3\theta_A\right)} \times \qquad \text{(B24)}$$
$$\left(e^{2\tan(\varphi)\theta_B}\left(2\tan(\varphi)\cos(\theta_B) + \sin(\theta_B)\right) - e^{2\tan(\varphi)\theta_A}\left(2\tan(\varphi)\cos(\theta_A) + \sin(\theta_A)\right)\right)$$

$$g'_{35} = \frac{5}{4}\frac{\left(\alpha^2+\beta^2\right)^2}{16\tan^2(\varphi)+1}e^{-4\tan(\varphi)\theta_A} \times$$
$$\left(e^{4\tan(\varphi)\theta_B}\left(4\tan(\varphi)\cos(\theta_B)+\sin(\theta_B)\right)-e^{4\tan(\varphi)\theta_A}\left(4\tan(\varphi)\cos(\theta_A)+\sin(\theta_A)\right)\right) \quad \text{(B25)}$$

The second integral that appears in the work rate of seismic acceleration reads

$$\iiint_{V_{J2}}\left(-k_h\gamma \underline{e}_z\right).\left(-\omega r\underline{e}_\theta\right)dV = k_h\gamma\omega D^4 g'_4 \quad \text{(B26)}$$

Non-dimensional function g'_4 is expressed as

$$g'_4 = 2\int_{\theta=\theta_C}^{\theta_A} g^2\cos(\theta)\left[\frac{f^2}{2}\left[t_0-\cos(t_0)\sin(t_0)\right]+\frac{2}{3}f\,g\sin^3(t_0)+\frac{g^2}{8}\left(t_0-\frac{\sin(4t_0)}{4}\right)\right]d\theta \quad \text{(B27)}$$

The integral written above is numerically calculated.
The work rate of pressure σ_T is given by

$$P_{\sigma_T} = \iint_{\Sigma}\left(\sigma_T\underline{e}_z\right).\left(-\omega r\underline{e}_\theta\right)d\Sigma \quad \text{(B28)}$$

The intersection between the tunnel and the horn is a curve which is symmetric with respect to $\left(O,\underline{e}_y\right)$ axis. A point M that belongs to that curve is characterized by

$$\underline{OM} = D\left[\left(\beta+\frac{1}{2}\right)-\alpha\frac{\cos(\theta)}{\sin(\theta)}\right]\underline{e}_y \pm Dg(\theta)\left[1-\left(\frac{\frac{\alpha}{\sin(\theta)}-f(\theta)}{g(\theta)}\right)^2\right]^{\frac{1}{2}}\underline{e}_Z \quad \text{(B29)}$$

Considering the above equation, the power of pressure σ_T reads

$$P_{\sigma_T} = -\sigma_T\omega D^3 g_5 \quad \text{(B30)}$$

Non dimensional function g_5 writes

$$g_5 = 2\alpha^2\int_{\theta=\theta_C}^{\theta_A}\frac{\cos(\theta)}{\sin^3(\theta)}g(\theta)\sin\left(t_0(\theta)\right)d\theta \quad \text{(B31)}$$

The integral given above is numerically calculated.

Appendix C. 2D rotational horn-like failure mechanism

$$h_1 = h_{11} + h_{12} \tag{C1}$$

$$h_{11} = \frac{\alpha^3}{3\sin^3(\theta_C)}\left[\frac{-e^{3\tan(\varphi)(\theta_C-\theta_A)}\left(\cos(\theta_A)+3\tan(\varphi)\sin(\theta_A)\right)+\left(\cos(\theta_C)+3\tan(\varphi)\sin(\theta_C)\right)}{9\tan^2(\varphi)+1}\right] \tag{C2}$$

$$h_{12} = \frac{\alpha^3}{3}\left[\frac{\cos(\theta_A)}{\sin(\theta_A)} - \frac{\cos(\theta_C)}{\sin(\theta_C)}\right] \tag{C3}$$

With

$$\alpha = \frac{\tan(\theta_C)\tan(\theta_A)}{\tan(\theta_A)-\tan(\theta_C)} \tag{C4}$$

$$h_2 = h_{21} + h_{22} \tag{C5}$$

$$h_{21} = \frac{\alpha^3}{3\sin^3(\theta_C)}\left[\frac{-e^{3\tan(\varphi)(\theta_C-\theta_B)}\left(\cos(\theta_B)+3\tan(\varphi)\sin(\theta_B)\right)+e^{3\tan(\varphi)(\theta_C-\theta_A)}\left(\cos(\theta_A)+3\tan(\varphi)\sin(\theta_A)\right)}{9\tan^2(\varphi)+1}\right] \tag{C6}$$

$$h_{22} = -\frac{\alpha^3}{3\sin^3(\theta_A)}\left[\frac{e^{3\tan(\varphi)(\theta_B-\theta_A)}\left(-\cos(\theta_B)+3\tan(\varphi)\sin(\theta_B)\right)-\left(-\cos(\theta_A)+3\tan(\varphi)\sin(\theta_A)\right)}{9\tan^2(\varphi)+1}\right] \tag{C7}$$

$$h_3 = h_{31} + h_{32} \tag{C8}$$

$$h_{31} = \frac{\alpha^3}{3\sin^3(\theta_C)}\left[\frac{e^{3\tan(\varphi)(\theta_C-\theta_A)}\left(\sin(\theta_A)-3\tan(\varphi)\cos(\theta_A)\right)-\left(\sin(\theta_C)-3\tan(\varphi)\cos(\theta_C)\right)}{9\tan^2(\varphi)+1}\right] \tag{C9}$$

$$h_{32} = \frac{\alpha^3}{6}\left[\frac{1}{\sin^2(\theta_A)} - \frac{1}{\sin^2(\theta_C)}\right] \tag{C10}$$

$$h_4 = h_{41} + h_{42} \tag{C11}$$

$$h_{41}=\frac{\alpha^{3}}{3\sin^{3}\left(\theta_{C}\right)}\left[\frac{e^{3\tan(\varphi)(\theta_{C}-\theta_{B})}\left(\sin\left(\theta_{B}\right)-3\tan\left(\varphi\right)\cos\left(\theta_{B}\right)\right)-e^{3\tan(\varphi)(\theta_{C}-\theta_{A})}\left(\sin\left(\theta_{A}\right)-3\tan\left(\varphi\right)\cos\left(\theta_{A}\right)\right)}{9\tan^{2}\left(\varphi\right)+1}\right] \tag{C12}$$

$$h_{42}=-\frac{\alpha^{3}}{3\sin^{3}\left(\theta_{A}\right)}\left[\frac{e^{3\tan(\varphi)(\theta_{B}-\theta_{A})}\left(3\tan\left(\varphi\right)\cos\left(\theta_{B}\right)+\sin\left(\theta_{B}\right)\right)-\left(3\tan\left(\varphi\right)\cos\left(\theta_{A}\right)+\sin\left(\theta_{A}\right)\right)}{9\tan^{2}\left(\varphi\right)+1}\right] \tag{C13}$$

$$h_{5}=\beta+\frac{1}{2} \tag{C14}$$

$$\beta=\frac{\tan\left(\theta_{C}\right)}{\tan\left(\theta_{A}\right)-\tan\left(\theta_{C}\right)} \tag{C15}$$

$$h_{6}=\frac{\alpha^{2}}{2\tan\left(\varphi\right)\sin^{2}\left(\theta_{A}\right)}\left[e^{2\tan(\varphi)(\theta_{B}-\theta_{A})}-1\right] \tag{C16}$$

$$h_{7}=\frac{\alpha^{2}}{2\tan\left(\varphi\right)\sin^{2}\left(\theta_{C}\right)}\left[1-e^{2\tan(\varphi)(\theta_{C}-\theta_{B})}\right] \tag{C17}$$